

# Turbulent clustering of initially well-mixed buoyant particles on a free-surface by Lagrangian coherent structures

Kenneth R. Pratt,<sup>a)</sup> Aaron True,<sup>b)</sup> and John P. Crimaldi<sup>c)</sup>

*Department of Civil, Environmental and Architectural Engineering, University of Colorado, Boulder, Colorado 80309-0428, USA*

(Received 12 January 2017; accepted 15 June 2017; published online 6 July 2017)

Particles that float on the surface of a 3D incompressible turbulent flow are exposed to non-divergence-free properties that result in clustering and unmixing, a reversal of how turbulence normally acts to mix and dilute scalars. Particle clustering is dominated by Lagrangian processes that depend on the time history of the flow; this suggests that Lagrangian coherent structures (LCS) might serve as templates for cluster formation. In this study, non-divergence-free clustering is examined both experimentally and numerically to elucidate the role of LCS in the formation of particle clusters and voids. Experiments are performed on the free-surface of a water-filled tank with turbulence driven by the random pulsing of centrifugal pumps on the tank bottom. Clustering is quantified by imaging fluorescent, buoyant particles that are placed in an initially random distribution on the free-surface. Within clusters, concentrations are observed to increase by an order of magnitude, with the likelihood of observing enhanced concentrations increasing by two orders of magnitude. LCS, obtained from velocity fields utilizing particle image velocimetry, are shown to act as templates for cluster formation. In addition, LCS are shown to possess a dilatation component in non-divergence-free flows that is responsible for unmixing. Numerically, a non-divergence-free chaotic model consisting of interacting Taylor vortices is utilized to investigate processes responsible for cluster formation seen in the experiments. The model results support the experimental finding that LCS act as templates for particle clusters, with scalar unmixing driven by the dilatation component. *Published by AIP Publishing.* [<http://dx.doi.org/10.1063/1.4990774>]

## I. INTRODUCTION

Initially well-mixed buoyant particles that are confined to float on the surface of a 3D incompressible turbulent flow have been shown to cluster due to the non-divergence-free behavior.<sup>1-3</sup> This non-divergence-free behavior results from the fact that particles are constrained to move within a single 2D surface of the 3D flow. Concentrations of scalars can increase significantly within the clusters, which can have a number of consequences, ranging from increased reaction rates to altered predator/prey relations for clustering biota. A simple example of this behavior on the free-surface of the ocean is the Langmuir circulation<sup>4</sup> where floating scalars (e.g., bubbles and seaweed) tend to flee from areas of upwelling (divergence zone) and aggregate in areas of downwelling (convergence zone), forming long streaks on the ocean surface.

The transport of particles in non-divergence-free flows differs significantly from that of scalars transported in divergence-free flows. In divergence-free flows, turbulence promotes scalar dilution through repeated stretching and folding of fluid elements that enhances molecular diffusion.<sup>5,6</sup> Turbulence, therefore, is recognized for its ability to mix and dilute initial concentrations of scalars due to rapid stirring. The arrow of time for incompressible chaotic advection, how-

ever, can only point in one direction, as it is not possible for initially well-mixed passive scalars to unmix and form clusters.<sup>7</sup>

There are two situations, however, that can result in particle unmixing. The first occurs in incompressible divergence-free flows in instances where scalars do not faithfully follow streamlines of the flow.<sup>8</sup> Inertial particles<sup>9</sup> and gyrotactic phytoplankton,<sup>10</sup> for example, have been shown to exhibit clustering behavior, even though they are transported by a divergence-free flow. While this scenario occurs in an incompressible environment, it can be interpreted in terms of an effective compressibility, as the drift velocity of the particles results in an effectively compressible velocity field. This scenario has also been observed in particles undergoing diffusiophoresis while exposed to a chaotic flow.<sup>11</sup> The second situation involves particles that follow the streamlines of the flow but are transported by a compressible velocity field. Particles confined to the free-surface of an incompressible 3D flow, for example, are following the streamlines of a 2D compressible velocity field.

Previous studies have examined this latter behavior using both experiments and numerics. Cressman *et al.*<sup>1</sup> quantified clustering on the surface of a water-filled tank ( $Re = 160$ ) using virtual particles in addition to using real particles to visually show increases in particle density. In addition, the mean square separation between particles on the free-surface showed a reduced scaling exponent compared to the classical Richardson value. A later study expanded upon this using

<sup>a)</sup>Electronic mail: kenneth.pratt@colorado.edu

<sup>b)</sup>Electronic mail: aaron.true@colorado.edu

<sup>c)</sup>Electronic mail: john.crimaldi@colorado.edu

a similar technique to track the time evolution of the fractal dimension and discussed how an initially uniform distribution of particles can aggregate and form a fractal structure.<sup>12</sup> A result of this clustering is an enhancement in particle concentrations, with concentration probability density functions (PDFs) exhibiting a power law decay that is dependent on the scale of sampling.<sup>13</sup> These studies used velocity fields obtained experimentally using particle image velocimetry to advect virtual particles with zero size and mass. This study expands upon this previous work by quantifying clustering using real particles in experimental flows.

Numerically, Boffetta *et al.*<sup>8</sup> studied the effect of finite-time correlations of the surface velocity field on the formation of clusters. They found that the extent of clustering is influenced by time correlations of the flow, with an enhancement/reduction in clustering dependent upon the compressibility of the system. A subsequent study verified this experimentally.<sup>14</sup> Recently, Lovecchio *et al.*<sup>15</sup> used direct numerical simulation (DNS) to study the time persistence of floating clusters in relation to the fluid time scales. They found that clusters outlive the Eulerian turbulent structures that produced them, indicating that the instantaneous divergence field alone is not sufficient to capture the formation of the cluster's fractal structure. To capture this long-term clustering, a Lagrangian approach is needed.

Huntley *et al.*<sup>16</sup> have shown that regions of dilatation (a Lagrangian based metric of quantifying area changes) can be correlated with cluster strength. In addition, they showed that the finite-time Lyapunov exponent (FTLE) field for non-divergence-free flows can be decomposed into stretching and dilatation terms. This decomposition separates shape-changing processes (due to stretching) from area-changing processes (due to dilatation). The dilatation rate, therefore, can be used as a diagnostic to predict where clusters will form. Dilatation alone, however, cannot account for how stretching can change the shape of clusters after they have been formed. To capture the full dynamics of cluster formation, both stretching and dilatation may need to be accounted for. Recently, clustering of scalars in simple numerical compressible flows has been linked with the presence of Lagrangian coherent structures.<sup>17</sup> How this behavior translates to systems with chaotic time-dependent divergence fields is still unknown.

Lagrangian analysis has become a useful tool because of the ability to track coherent structures that persist across space and time. As previously discussed, clustering persists over time periods longer than the time scale of the Eulerian structures that initially formed them, such as areas of convergence in downwelling zones. Clusters will be formed by areas of convergence, but deformed by the persistent stretching and folding that occurs in chaotic, turbulent flows. Lagrangian coherent structures (LCS) are defined as material lines or surfaces that highlight the most repelling and attracting regions of the fluid flow.<sup>18</sup> Haller showed that these surfaces are analogous to the invariant unstable and stable manifolds of hyperbolic orbits in time-periodic chaotic systems.<sup>19</sup> Fluid parcels surrounding these surfaces can be either attracted or repelled from these surfaces at an exponential rate. These time-evolving surfaces have been described as the hidden skeleton of fluid flows because

of how they mold the complex patterns of a tracer, incorporating the complicated time history of stretching and folding.<sup>22</sup> In addition, these surfaces evolve in time and play a major role in the enhancement or inhibition of mixing,<sup>20,21</sup> including acting as a template for the coalescence of scalars that were initially separated.<sup>23</sup> Much of the previous work on LCS, however, has been done in an incompressible context. More recently, studies have computed LCS in effectively compressible contexts, such as the transport of inertial particles.<sup>25–27</sup> The aim of this study is to infer the role that Lagrangian coherent structures play in the clustering of scalars on an effectively compressible free-surface, which thus far has received little attention.<sup>16,17</sup>

A standard technique for locating these repelling and attracting surfaces, whether in a compressible or incompressible context, is the finite-time Lyapunov exponent (FTLE). The FTLE is a scalar field that is computed by advecting a uniform grid of tracers either forward (for repelling surfaces) or backward (for attracting surfaces) in time over an integration time  $T$ . The resulting rate at which neighboring particles have contracted or separated is calculated at each grid point. LCS are extracted from this field by locating the ridge lines of the FTLE field. It should be noted, however, that the FTLE field can falsely locate regions of high shear that are not true LCS, and has been described as heuristic in a recent review by Haller.<sup>18</sup> Other issues include missing LCS due to numerical resolution, in addition to the finite-time LCS being misaligned from the unstable/stable manifold. In this study, however, we are interested in locating surfaces of persistent straining and deformation, which is what strong ridges of the FTLE indicate.

## II. EXPERIMENTAL TECHNIQUE

Clustering statistics of fluorescent buoyant particles on a turbulent free-surface are collected in a laboratory turbulence facility. Particle fluorescence is excited by a laser and imaged from above using a CCD camera. From discretized particle locations, clustering statistics are computed for both turbulent and quiescent cases. In addition, particle image velocimetry (PIV) is used to quantify the turbulence characteristics on and below the free-surface. Aspects of the experimental technique are discussed in turn below.

### A. Turbulence tank

Experiments were performed in a  $60 \times 60 \times 60$  cm water-filled glass tank that is open at the top such that there is a free-surface (Fig. 1). Turbulence is generated from below using a  $6 \times 6$  randomly actuated synthetic jet array (RASJA) that has been shown previously to produce large regions of homogeneous and isotropic turbulence.<sup>28</sup> The RASJA is fired in a spatiotemporal random pattern (discussed in Sec. II B) that creates 3D turbulence in the upper region of the tank, driving a turbulent free-surface flow. Each of the 36 vertical jets is independently driven by submerged centrifugal pumps (Rule 360 gph 12 V DC bilge pumps). The jet spacing is 10 cm and the pump inlets and outlets are located 4 cm and 7 cm above the tank bottom, respectively. The distance between the jet orifices and free-surface is 49 cm; this

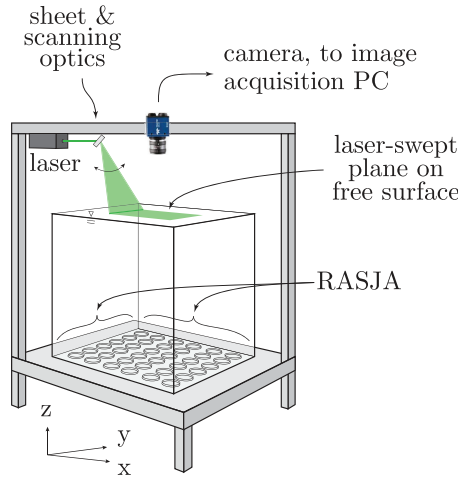


FIG. 1. Schematic of the tank design and laser/camera setup. A  $60 \times 60$  cm water-filled glass tank is leveled on a steel frame. The RASJA, composed of 36 pumps, rests on the tank bottom. The laser (green) used to fluoresce particles on the free-surface is spread into a sheet and scanned along the free-surface. The camera used to image fluorescent particles is mounted 50 cm above the tank free-surface.

is sufficiently large to allow jets to merge before they reach the free-surface, thereby eliminating upwelling events from single jets. The experiments were conducted with salt water (100 ppt) to provide sufficient buoyancy for the particles. The free-surface is skimmed before each experimental trial in order to keep the surface clean, as exposure to air and other contaminants have been shown to interfere with free-surface transport.<sup>1,28</sup>

## B. Generation of turbulence

The RASJA design is based on that of Variano and Cowen<sup>28</sup> but smaller in size ( $6 \times 6$  vs.  $8 \times 8$ ). The pumps are powered using a 20 A adjustable DC power supply and individually switched using transistor-transistor logic (TTL) signals generated using a LabVIEW code paired with a digital output card (PCIe-6509). The TTL signals command MOSFET transistors (N-Channel) to supply DC power to the pumps.

We used the spatiotemporal jet driving pattern found to be optimal by Variano and Cowen (Fig. 2): Each jet operates independently of the others and is triggered randomly for a duration ( $d_{on}$ ) chosen from a normal distribution ( $f_{on}$  centered on  $\mu_{on} = 1$  with standard deviation  $\sigma_{on} = 0.25$ ) and then is turned off for a duration ( $d_{off}$ ) drawn from a normal distribution ( $f_{off}$  centered on  $\mu_{off} = 10$  with standard deviation  $\sigma_{off} = 3$ ). This process is then repeated by continuously sampling on/off times from these normal distributions for all 36 pumps.

## C. Imaging of fluorescent particles for clustering analysis

The free-surface of the flow is seeded with buoyant particles that are subsequently imaged for clustering behavior. The particles (Cospheric UVPMS-BR-0.995) are fluorescent red polyethylene microspheres with a density of 0.995 g/cc and a diameter of 125  $\mu\text{m}$ . Particles are sufficiently buoyant in the

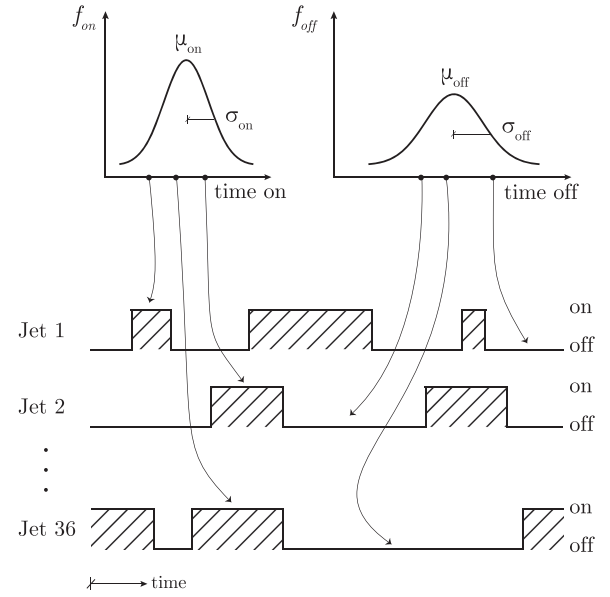


FIG. 2. Algorithm for pump firing. On and off times are drawn randomly and independently for each pump from normal distributions  $f_{on}$  and  $f_{off}$ , respectively.  $f_{on}$  has mean  $\mu_{on} = 1$  s and standard deviation  $\sigma_{on} = 0.25$  s.  $f_{off}$  has mean  $\mu_{off} = 10$  s and standard deviation  $\sigma_{off} = 3$  s.

100 ppt salt water that they remain on the surface for the entire range of turbulence intensities tested. Because the particles are hydrophobic, they are initially wetted with a small volume of surfactant (Cospheric Tween 80). Furthermore, to mitigate particle interactions due to surface tension, a small amount of miscible surfactant (25 ml of Dawn dish detergent) is added to the salt water in the tank. Clustering results were insensitive to the addition of surfactant beyond the small amount required to prevent clumping. Approximately 50 percent of the particle is submerged in the water, leaving approximately 60  $\mu\text{m}$  exposed to the air and 60  $\mu\text{m}$  submerged within the water. The forces caused by particle-air friction are negligible compared to the forces of the underlying turbulent flow. In addition, the 60  $\mu\text{m}$  that are submerged in the water are representative of the surface layer, as dissipation scales exceed that size by an order of magnitude.

Particle fluorescence is excited using a 200 mW 514 nm continuous-wave (CW) laser. The beam is spread into a horizontal sheet using a cylindrical lens and then scanned along the free-surface by a scanning mirror (Fig. 1). Particles are imaged in a central 16 cm  $\times$  12 cm region to avoid wall effects. Images are captured at 1 Hz with an Imperx Bobcat 1410 CCD camera fitted with a 25 mm lens; a bandpass filter is used to image only the particle fluorescence. The locations of these particles are discretized using a standard peak finding algorithm. A LabVIEW program is used to synchronize the image acquisition with the light sheet scan.

Wetted particles are initially distributed on a quiescent free-surface. Images are taken in this quiescent state to show that the initial particle distribution is random. For each turbulence case, the RASJA device was activated and 120 images were collected after a 30-s transient period. This procedure was replicated 9 times for each case to produce ensemble clustering statistics and various statistics are computed using these discretized locations.

## D. Quantifying clustering

We use two approaches for quantifying particle concentration distributions based on discrete particle locations. The first, Voronoï tessellation,<sup>29</sup> is a scale-invariant approach that we use to compute concentration distributions that are independent of interrogation scale.<sup>10</sup> Voronoï tessellation produces polygons around each particle with a resulting concentration equal to the inverse polygon area. Tessellation polygons at the image boundary can have diverging vertices with an undefined area and were excluded from the analysis. The second clustering approach, Monte Carlo concentration sampling,<sup>30</sup> is a scale-dependent approach that we use to determine characteristic clustering scales. In the Monte Carlo approach, an interrogation region consisting of a circle of diameter  $d$  is placed randomly in the domain and the resulting particle concentration is computed. The domain is interrogated repeatedly with this process until the computed concentration distribution is statistically converged. If a distribution of particles is indeed random, the probability density function of the resulting concentrations using this approach will produce a Poisson distribution.<sup>30,31</sup> Deviations from randomness due to unmixing will result in a non-Poisson distribution.

The Monte Carlo concentration distributions can be used to compute the clustering index ( $CI$ ) at a given circle size  $d$ ,

$$CI(d) = \frac{\sigma_c - \sigma_p}{\mu_p}, \quad (1)$$

where  $\sigma_c$  is the standard deviation of the clustered concentration distribution, and  $\sigma_p$  and  $\mu_p$  are the standard deviation and mean from the Poisson concentration distribution, respectively. The clustering index for a range of  $d$  values is then computed, and the circle size that produces a maximum  $CI$  is identified as a characteristic scale of clustering.

## E. Calculating finite-time Lyapunov exponents and the dilatation rate

Backward finite-time Lyapunov exponents are computed for both the experimental and numerical flows using the method of Shadden *et al.*<sup>32</sup> A flow map  $\phi_{t_0}^{t_0-T}$  is generated by advecting an initially uniform array of points ( $425 \times 645$  for the experimental flow and  $401 \times 401$  for the Taylor vortex flow) backwards from  $t = t_0$  over an integration time  $T$ . The integration time  $T$  is typically chosen depending upon the physics of the flow, such as the period. For a non-periodic system, this choice is not as straightforward. Choosing too long of an integration time will result in manifolds that become space-filling, while too short will not capture the appropriate dynamics of the flow. For this study, we choose an integration time that is sufficient to capture the clustering processes, which is approximately the time that it takes to form compact clusters from an initially well-mixed state of particles. The time that it takes to form a cluster, and the corresponding integration time, will therefore depend upon the compressibility of the system. Non-dimensional integration times for the experimental and numerical flows are  $t^* = 3.6$  and  $t^* = 6.4$ , respectively. Times are non-dimensionalized by multiplying by the maximum Lagrangian dilatation rate

observed in the flow,  $t^* = t\delta_{max}$ . Integration times for the experimental flows were shorter due to experimental constraints. Approximate derivatives of  $\phi_{t_0}^{t_0-T}$  with respect to initial conditions are computed using centered finite differences to generate the so-called right Cauchy-Green deformation tensor

$$\Delta = \frac{d\phi_{t_0}^{t_0-T}(\mathbf{x})}{d\mathbf{x}} \frac{d\phi_{t_0}^{t_0-T}(\mathbf{x})}{d\mathbf{x}}.$$

Finally, the FTLE is computed as

$$\sigma_{t_0}^T(\mathbf{x}) = \frac{1}{T} \ln(\lambda_{max}(\Delta)), \quad (2)$$

where  $\lambda_{max}(\Delta)$  is the maximum eigenvalue of  $\Delta$ . The topological ridge lines of the spatial distribution of the FTLE field correspond to attracting LCS, a region of strain which attracts nearby particle trajectories.

The Lagrangian dilatation rate (LDR) is a metric that is equal to the average divergence experienced by a particle along its trajectory.<sup>16</sup> This corresponds to the rate at which material volumes are contracting or expanding over time. For incompressible flows, the dilatation rate is equal to zero, signifying an area preserving flow. Non-divergence-free flows, however, consist of regions of both expansion and contraction of fluid volumes, and therefore a non-zero dilatation rate. To compute the Lagrangian dilatation rate, a uniform grid of particles are advected backward in time for an integration time  $T$ , and the integral is taken along the trajectory for each particle. The Lagrangian dilatation rate  $\delta$  is then computed as

$$\delta(\mathbf{x}) = \frac{1}{T} \int_{t_0}^{t_0-T} \nabla \cdot \mathbf{u}(\mathbf{x}(\tau), \tau) d\tau. \quad (3)$$

In non-divergence-free flows, the FTLE field is equal to the average of the stretching and dilatation rates.

## F. Particle image velocimetry

Planar particle image velocimetry (PIV) data were collected both on the free-surface (x-y plane) and within the water column (x-z plane) to characterize fluid turbulence at varying intensities. The tank was seeded with neutrally buoyant, low Stokes number particles (20  $\mu\text{m}$ , 1.03 g/cc, polyamide microspheres, Dantec Dynamics PSP-20) at densities sufficient to populate interrogation subwindows with 8–10 particles at the given optical magnification. Particles were pre-wetted using a surfactant and mixed uniformly in the entire tank. A 200 mW CW laser (514 nm) beam was spread into a thin sheet ( $\sim 1$  mm) using a cylindrical diverging lens. For water column (x-z plane) data sets, the light sheet was oriented perpendicular to the free-surface illuminating a 10 cm deep plane beginning at the free-surface (13 cm wide). For free-surface (x-y plane) data sets, the light sheet illuminated a 12 cm  $\times$  16 cm plane on the free-surface centered in the tank to minimize wall effects. For all data sets, a CCD camera (IMPERX Bobcat 1410M, 1040  $\times$  1392) imaged seeding particles in the light sheet at frame rates selected to optimize particle displacements (10–15 Hz depending on turbulence intensities) at one-quarter to one-half the width of an interrogation subwindow for the given optical magnification (115  $\mu\text{m}/\text{pixels}$ ).

15-min image time series were postprocessed using DaVis software (8.2.3, Lavisoin, Inc.) first to improve particle fidelity via background subtraction and subsequently to compute planar fluid velocity fields. Fast-fourier transform (FFT) based cross-correlation analyses were used to compute particle displacements within interrogation subwindows between successive image frames. Multi-pass cross-correlation schemes with overlapping (50%–75%) interrogation subwindows of decreasing sizes (264 pixels–64 pixels) ensured statistically valid correlation peak finding and resulting particle displacement computations. The resulting velocity fields (with spatial resolution of 1.85 mm/vector) provided time-resolved measurements of fluid turbulence at varying intensities, quantifying both statistical and instantaneous turbulence characteristics.

### III. RESULTS

#### A. Characterization of turbulence in experimental facility

Clustering is investigated for three different turbulence conditions in the RASJA facility (Table I). Turbulence is controlled by modulating voltage to the pumps, which controls the pump speed. Resulting turbulence can be characterized by the Taylor Reynolds number

$$Re_\lambda = \frac{u_{rms}\lambda}{\nu}, \quad (4)$$

where

$$\lambda = \sqrt{\frac{u_{rms}^2}{\left\langle \left( \frac{\partial u}{\partial x} \right)^2 \right\rangle}}, \quad (5)$$

and turbulent kinetic energy (TKE) dissipation rate (estimated for isotropic, homogeneous turbulence, which accounts for the factor of 10 in front)<sup>13</sup>

$$\epsilon = 10\nu \left\langle \left( \frac{\partial u}{\partial x} \right)^2 \right\rangle, \quad (6)$$

where  $\nu$  is the kinematic viscosity ( $1 \times 10^{-6}$  m<sup>2</sup>/s). Furthermore, the compressibility of the free-surface can be characterized by a nondimensionalized mean square divergence<sup>1</sup>

$$\zeta = \frac{\left\langle \left( \frac{\partial u}{\partial x} + \frac{\partial v}{\partial y} \right)^2 \right\rangle}{2 \left\langle \left( \frac{\partial u}{\partial x} - \frac{\partial v}{\partial y} \right)^2 \right\rangle}. \quad (7)$$

Higher  $Re_\lambda$  leads to increased compressibility on the free-surface. Statistics in Table I have been both spatially and

TABLE I. Turbulence parameters [Taylor Reynolds number ( $Re_\lambda$ ), TKE dissipation rate ( $\epsilon$ ), the Taylor microscale ( $\lambda$ ), and the flow compressibility ( $\zeta$ )] for the three flow conditions in the experimental study.

$Re_\lambda$	Pump voltage (V)	$\epsilon$ (cm <sup>2</sup> /s <sup>3</sup> )	$\lambda$ (cm)	$\zeta$
130	4	0.02	1.8	0.19
230	6	0.07	1.7	0.23
350	8	0.16	1.7	0.34

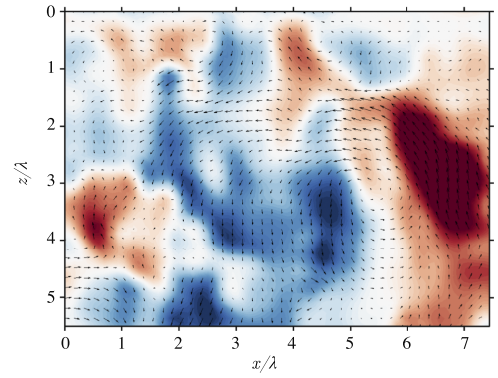


FIG. 3. Representative instantaneous velocity field (vectors) and vertical velocity magnitude (colors) for a vertical slice extending downward from the free-surface at  $Re_\lambda = 130$ . Red indicates areas of upwelling while blue indicates areas of downwelling. Magnitudes range from  $-3$  to  $3$  cm/s.

temporally averaged to arrive at the mean quantity for each pump voltage. Gradients are computed through the DaVis software at each grid point via the strain tensor. With calculated dissipation scales ranging between 0.5 and 0.85 mm, and a spatial resolution of 1.85 mm/vector, these gradients are sufficient to capture the velocity gradients on the order of the dissipation scale.

Representative snapshots of the resulting turbulence field at  $Re_\lambda = 130$  are shown in a vertical plane intersecting the free-surface (Fig. 3) and a horizontal plane at the free-surface (Fig. 4). Due to experimental constraints, these snapshots were taken at different times. In both figures, arrows indicate instantaneous velocity vectors in the plane. In the vertical plane (Fig. 3), the vertical component of the velocity is depicted, where red indicates regions of upwelling and blue indicates regions of downwelling. Closer to the free-surface, velocities have attenuated, but large regions of upwelling and downwelling are still evident. These regions drive the turbulence on the free-surface and are associated with areas of convergence and divergence, as shown at a different instant of time in Fig. 4. The associated divergence field is depicted, where green indicates regions of convergence and purple indicates regions of divergence. As expected, the divergence field on the free-surface is non-zero.

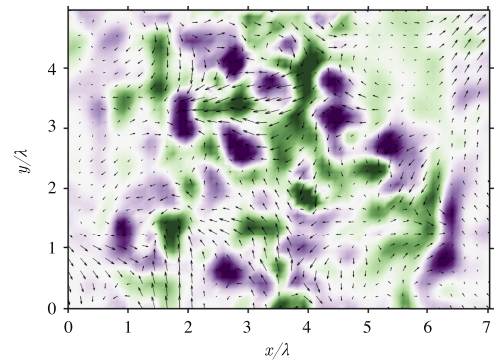


FIG. 4. Representative instantaneous velocity field (vectors) and divergence field (colors) at the free-surface for  $Re_\lambda = 130$ . Green indicates regions of convergence while purple indicates regions of divergence. Magnitudes range from  $-1.25$  to  $1.25$  s<sup>-1</sup>.

## B. Clustering of initially well-mixed scalars: Experimental

### 1. Quantifying scale-independent clustering with Voronoï tessellation

As mentioned in Sec. II D, the Voronoï tessellation provides a scale invariant method of calculating concentration enhancement. The clustering of initially well-mixed particles is shown in Fig. 5 at an instant in time. Particles are well-mixed in the quiescent case (left) and exhibit clustering when exposed to turbulent free-surface flow (right). Particle locations are shown in Fig. 5(a) and the corresponding Voronoï tessellations are overlaid on particle location in Fig. 5(b). Particle concentrations from the Voronoï tessellations are shown in Fig. 5(c). Contour values range from  $C/C_0 = 0.5$  (light gray) to  $C/C_0 = 6$  (black), where  $C_0$  is the average well-mixed concentration. As the particles cluster due to non-divergence-free flow, corresponding concentrations within the clusters increase by an order of magnitude. These large areas of enhanced concentration (black) as well as voids (white) are evident on the turbulent free-surface.

The Voronoï tessellation is used to create probability density functions (PDF) of particle concentrations [Fig. 6(a)] for three turbulence levels (black lines) as well as the initially well-mixed case (blue line). There is an increased likelihood of observing both enhanced concentrations in the clusters ( $C/C_0 > 1$ ), as well as reduced concentrations in

the voids ( $C/C_0 < 1$ ). The concentration enhancement can be quantified as the ratio of the turbulent PDFs to the quiescent PDF [Fig. 6(b)]. Note that there is a 100-fold increase in the likelihood of observing both reduced and enhanced concentrations. It is evident that as turbulence intensities are increased, the extent of clustering also increases. These regions of enhanced concentrations, in addition to the increased prevalence of voids, can have profound impacts for biological and chemical systems. Predator/prey relations, for instance, can be impacted as the presence of clusters and voids will alter feeding rates, search strategies, and reaction rates. The extent of these impacts will depend upon the effective compressibility of the free-surface, which is dependent upon the overall turbulence intensities (Fig. 6).

### 2. Quantifying scale-dependent clustering with Monte Carlo sampling

While the Voronoï tessellation presented in Sec. III B 1 has the advantage of generating scale-independent particle concentrations, the scale at which clustering occurs may be of interest. To that end, we now employ the scale-dependent Monte Carlo approach discussed in Sec. II D to compute particle concentration PDFs [Fig. 7(a)]. PDFs are shown for the quiescent case (blue) and turbulent free-surface cases (gray and black). Although the total number of particles varied between flow cases, the diameter of the interrogation region ( $d$ ) was adjusted for each case such that it contained an average of 17

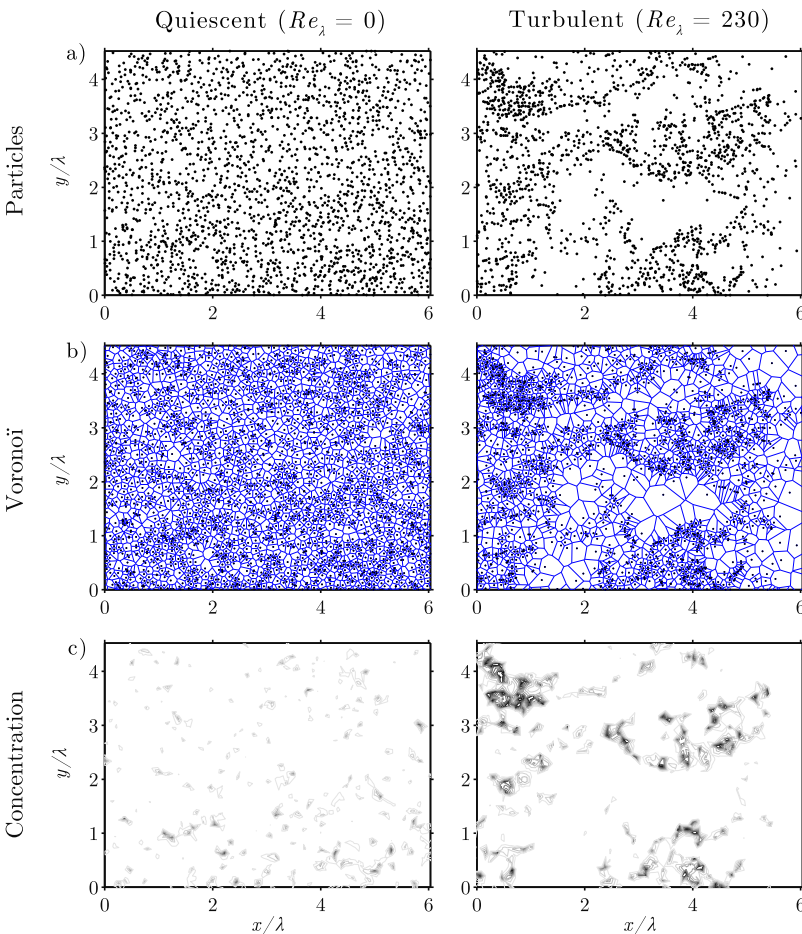


FIG. 5. Particle location and concentration for the quiescent case (left column) and turbulent case (right column). (a) Discretized particle locations (black) at a representative instant of time. (b) Voronoï tessellation (blue) superimposed on the discretized particle locations at the same time as (a). (c) Contours of concentration computed from Voronoï tessellation with values ranging from  $C/C_0 = 0.5$  (light gray) to  $C/C_0 = 6$  (black) at the same time as (a) and (b).

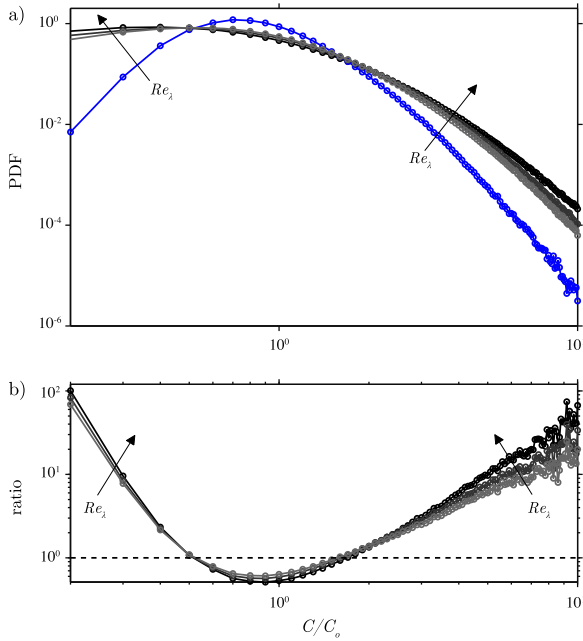


FIG. 6. (a) Particle concentration PDF computed from Voronoi tessellation for four flow cases:  $Re_\lambda = 350$  (black),  $Re_\lambda = 230$  (gray),  $Re_\lambda = 130$  (light gray), and the quiescent case (blue). (b) Turbulence concentration PDFs from (a) normalized by the quiescent case.

particles. Also shown (but difficult to discern) is the analytical Poisson distribution corresponding to  $\gamma = 17$ ; as expected this distribution almost exactly matches the quiescent data. This match indicates that the particles were indeed randomly distributed after being deposited on the free-surface. When the pumps are subsequently turned on, clustering is observed, as evidenced by the widening of the distributions, with increased probabilities of observing both enhanced/reduced concentrations. In addition, the width (standard deviation) of the distributions increase as turbulence levels are intensified, which indicates an increase in the intensity of clustering.

We can repeat this approach for a range of interrogation region sizes, and the standard deviation of the resulting PDFs can be used to compute clustering index [Eq. (1)] as a function of interrogation scale [Fig. 7(b)]. The interrogation scale has been normalized by the Taylor microscale [Eq. (5)]. For all cases, there is an identifiable interrogation scale at which  $CI$  reaches a maximum and then decays. Stronger turbulence lev-

els result in a larger clustering index. The scale at which this peak occurs corresponds to the approximate size of the clusters that are forming. For all turbulence intensities, this scale is smaller than the Taylor microscale ( $d/\lambda < 1$ ). At  $d/\lambda \ll 1$ , the curves collapse since sampling of the concentration field is occurring at a scale much smaller than the clusters. At  $d/\lambda \gg 1$ , sampling is occurring at scales much larger than the cluster, and the clustering index will asymptote to zero. It is not surprising that the scale at which maximum clustering occurs is the same order of magnitude as the Taylor microscale, as this is the characteristic scale of the flow that is inducing cluster formation.

### 3. Clustering on Lagrangian coherent structures

While free-surface clustering is often thought to coincide with downwelling regions, this is an Eulerian description that ignores the history of particle trajectories. A Lagrangian approach is a more natural means of elucidating clustering processes that permits cluster formation to be described in terms of Lagrangian coherent structures. To infer the influence of LCS on clustering, virtual particles (sizeless and massless) are advected using experimental velocity fields from the surface of the laboratory facility obtained using PIV. By using virtual particles, both the FTLE field and the concentration field can be computed simultaneously. Concentration contours of clustered virtual particles are computed for a random initial condition [Fig. 8(a)] and at two subsequent times as clusters form [Figs. 8(b) and 8(c)]. The backward-time FTLE field (left) computed at  $t_2$  [Fig. 8(d)] shows a striking similarity to the pattern of particle clustering at the same time in Fig. 8(c). The black lines (ridges) in the FTLE plot indicate regions of large strain and deformation, which correspond to attracting Lagrangian coherent structures. In addition, the compressible component ( $0 > \delta > -0.5 \text{ s}^{-1}$ ) of the dilatation field (right), computed at the same instant of time as the FTLE field, shows the same similarity.

To quantify the qualitative visual overlap seen for representative time snapshots in Fig. 8, Pearson correlation coefficients between particle concentrations and the FTLE, Lagrangian dilatation rate (LDR), and divergence metrics are computed as a function of time (Fig. 9). Correlation coefficients range from zero (no correlation) to unity (perfect correlation). Particles are initially well-mixed at  $t = 0$ , so the

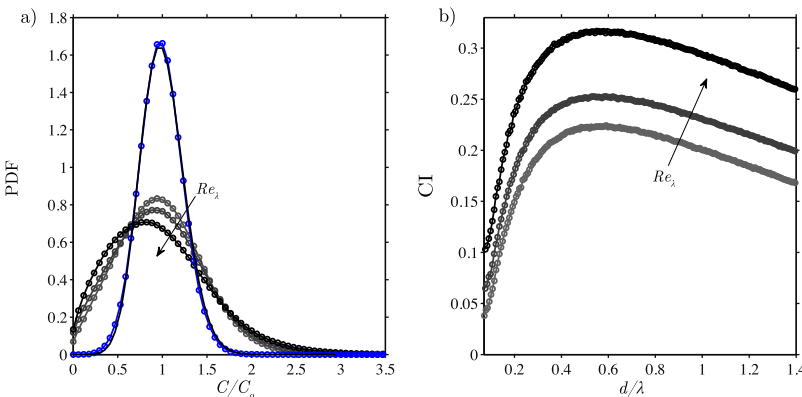


FIG. 7. (a) Concentration PDFs from the Monte Carlo technique for four flow cases:  $Re_\lambda = 0$  (blue),  $Re_\lambda = 130$  (light gray),  $Re_\lambda = 230$  (gray), and  $Re_\lambda = 350$  (black); also shown is the Poisson distribution with  $\gamma = 17$  (solid black). (b) Clustering index for turbulence cases as a function of interrogation scale, using same color coding as (a).

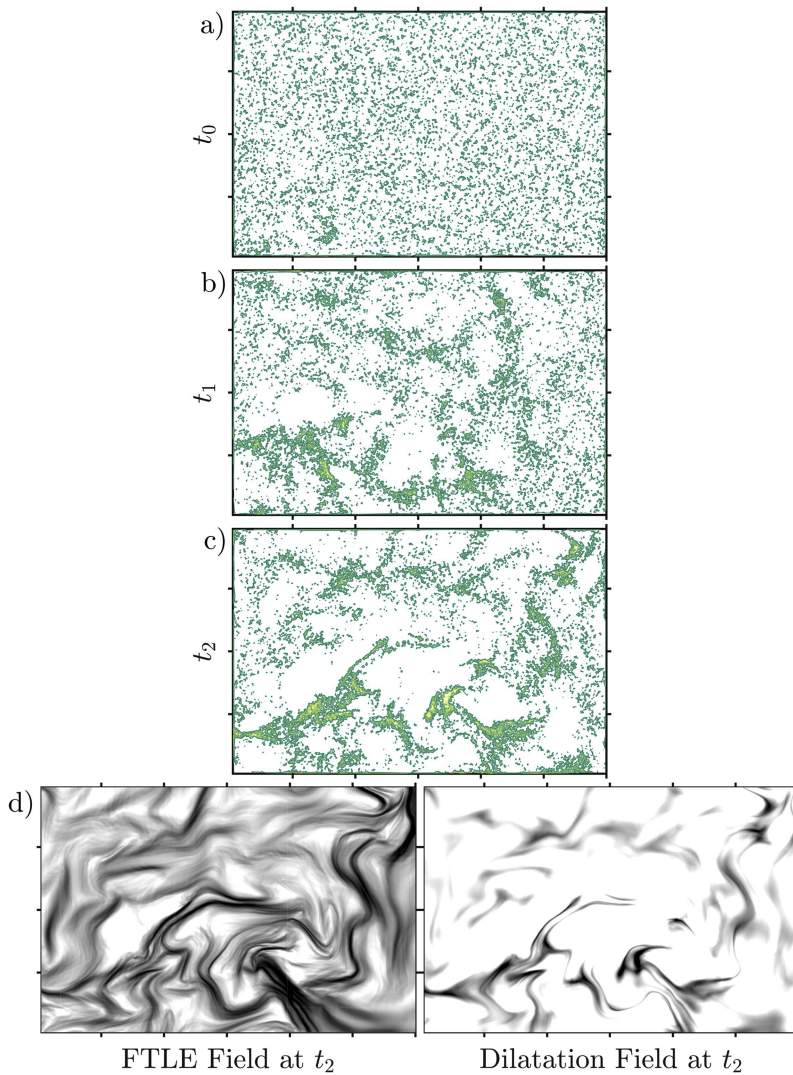


FIG. 8. [(a)–(c)] Concentrations of virtual particles using experimentally obtained free-surface velocities. Concentrations range from  $C/C_0 = 0.5$  (green) to  $C/C_0 = 3.5$  (yellow). The initial condition is shown in (a) with subsequent evolution shown in (b) and (c). (d) The FTLE field (left) and the compressible component ( $0 > \delta > -0.5$ ) of the dilatation field (right) corresponding to concentrations shown at  $t_2$  in (c).

Pearson correlation coefficient between particle concentration and all three of the metrics is initially zero. As particles begin to cluster (Fig. 8), the correlation between the particle concentration and the FTLE field grows strongly [Fig. 9(a)] and then asymptotes to a value of approximately 0.5; the maximum FTLE correlation is moderated by regions of stretching that do not induce particle clustering. An even stronger correlation is observed between the particle concentration and

the dilatation field [Fig. 9(b)], with a maximum value of 0.7. This indicates that, in this flow, dilatation is the dominant mechanism influencing scalar clustering and deformation (but can be captured by both the FTLE and LDR fields). Conversely, the behavior of the correlation between the particle concentration and the divergence field [Fig. 9(c)] is very different: this correlation reaches a peak value of only 0.3 and subsequently declines over time. This quantitatively shows

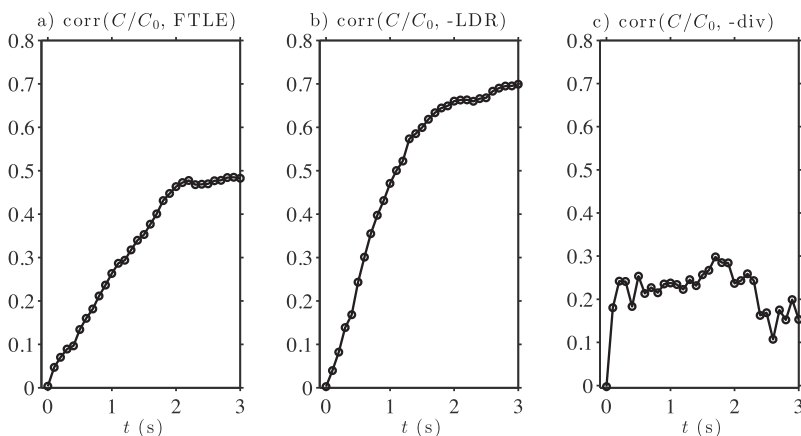


FIG. 9. 2D Pearson correlation coefficients for the experimental results between (a) particle concentration ( $C/C_0$ ) and FTLE, (b) particle concentration ( $C/C_0$ ) and Lagrangian dilatation rate (LDR), and (c) particle concentration ( $C/C_0$ ) and divergence field (div). Particles are initially well-mixed at  $t = 0$ . To make all correlations positive, the LDR and divergence field are multiplied by  $-1$ .

how the divergence field is unable to capture the important time history of particle clustering due to its Eulerian basis, while the Lagrangian metrics are better able to capture clustering.

The attracting LCS, therefore, acts as a template for the clustering of initially well-mixed scalars in non-divergence-free flows due specifically to the presence of the dilatation component. This cluster formation is inherently a Lagrangian process, as non-divergence-free velocity fields compress the scalar field, which results in clusters that are subsequently stretched and deformed along the LCS.

### C. Clustering of initially well-mixed scalars: Numerical

#### 1. Non-divergence-free Taylor vortex model

To further investigate the clustering seen in the above experimental data, we next turn to a numerical model to reinforce and expand upon the above work. To study the effects of non-divergence-free flows on particle clustering numerically, the interacting Taylor vortex model from Pratt *et al.*<sup>23</sup> was modified to include non-divergence-free behavior. From a dynamical systems perspective, the system of interacting Taylor vortices is both aperiodic and chaotic, a key component of turbulent systems, such as the turbulence tank used in the experimental section. For incompressible flows, this is one member of a family of exact vortex solutions to the Navier-Stokes equations<sup>24</sup> and is therefore representative of a turbulent, chaotic flow. The original divergence-free model consisted of a system of interacting Taylor vortices that result in a 2D incompressible chaotic flow. A Taylor vortex [Fig. 10(a)] centered at the origin has tangential velocity

$$u_\theta = Ur \exp\left(-\frac{r^2}{2r_0^2}\right), \quad (8)$$

where  $U$  is the strength of the vortex,  $r$  is the distance from its center, and  $r_0$  is the radius of the core. A final velocity field is then computed through the superposition of velocities from all vortices present in the flow. The vortices move in a square doubly periodic domain with size  $10r_0$ . For the model, 36 vortices with a radius  $r_0 = 1$  and strength  $U = \pm 0.75$  are placed randomly in the domain; the sign of  $U$  is chosen randomly for each vortex and determines rotation direction.

Motivated by the work of Pérez-Muñuzuri,<sup>17</sup> non-divergence-free effects are added to the model by incorporating a spatially periodic parameter,  $\rho(x, y)$ , that advects with and alters the velocity field of each Taylor vortex. This field is given by

$$\rho(x, y) = 1 + \kappa \sin(2\pi x/\Lambda) \sin(2\pi y/\Lambda),$$

where  $\kappa$  is a compressibility metric and  $\Lambda$  is the wavelength. For this study,  $\Lambda = 5r_0$ . The compressible velocity field [Fig. 10(b)] for each Taylor vortex is then

$$u_c = \frac{u_\theta}{\rho}. \quad (9)$$

This alteration is repeated for all 36 vortices that have been placed randomly in the domain. The velocity field, due to

the combined effects of these vortices, is the superposition of these individual vortex velocities at each grid point in the flow, computed from Eqs. (8) and (9) [Fig. 10(c)]. Vortices are advected by the superposed incompressible velocity at the vortex center ( $\mathbf{x}_1 = \mathbf{x}_0 + \mathbf{u}dt$ ) using a second-order improved Euler scheme. With this alteration, the compressible interacting Taylor vortex model is representative of the processes that are present on the free-surface of a turbulent flow, such as those seen in the experimental section. However, since this model does not contain an energy cascade, it is not a true turbulent system but is meant to simulate the fundamental processes of one, such as chaotic and aperiodic behavior.

Using the non-divergence-free Taylor vortex model, non-diffusive scalars are initialized in the well-mixed state and begin to cluster when exposed to the flow. Particles are advected in the same manner as the vortices, using a second-order improved Euler scheme. Figure 11(b) shows the resulting concentration contours at three times during cluster development; the contours range from  $C/C_0 = 0.5$  to  $C/C_0 = 6$ . The FTLE field [Fig. 11(a)] is overlaid on the concentration contours in Fig. 11(b), confirming that the FTLE, a Lagrangian metric, is capable of capturing this complex time history as clusters can be seen forming on the ridge lines (black), confirming results discussed in the experi-

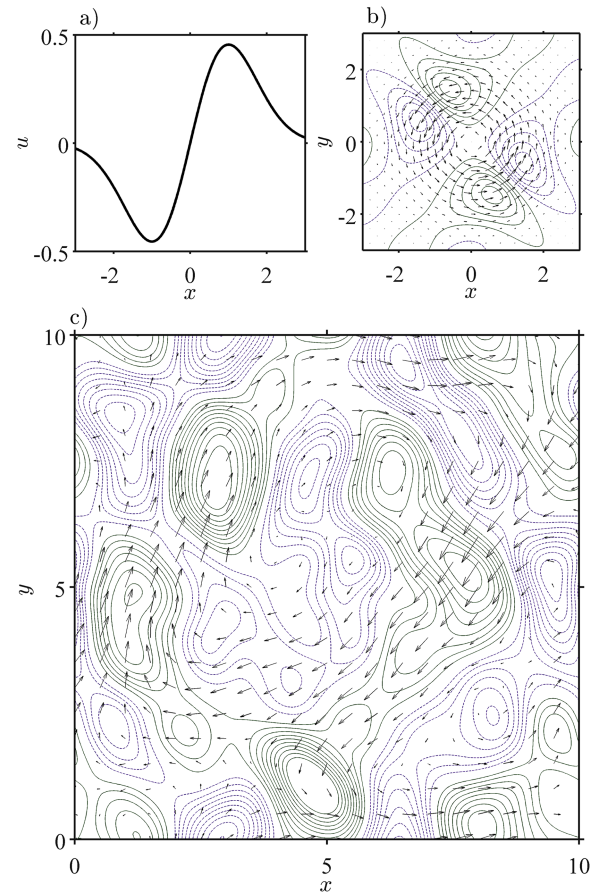


FIG. 10. (a) Horizontal transect of  $u_\theta$  for an incompressible Taylor vortex. (b) Velocity field (vectors) and divergence field (colored contours) for an individual compressible Taylor vortex. (c) A representative velocity field (vectors) and divergence field (colored contours) for the superposition of 36 compressible Taylor vortices.

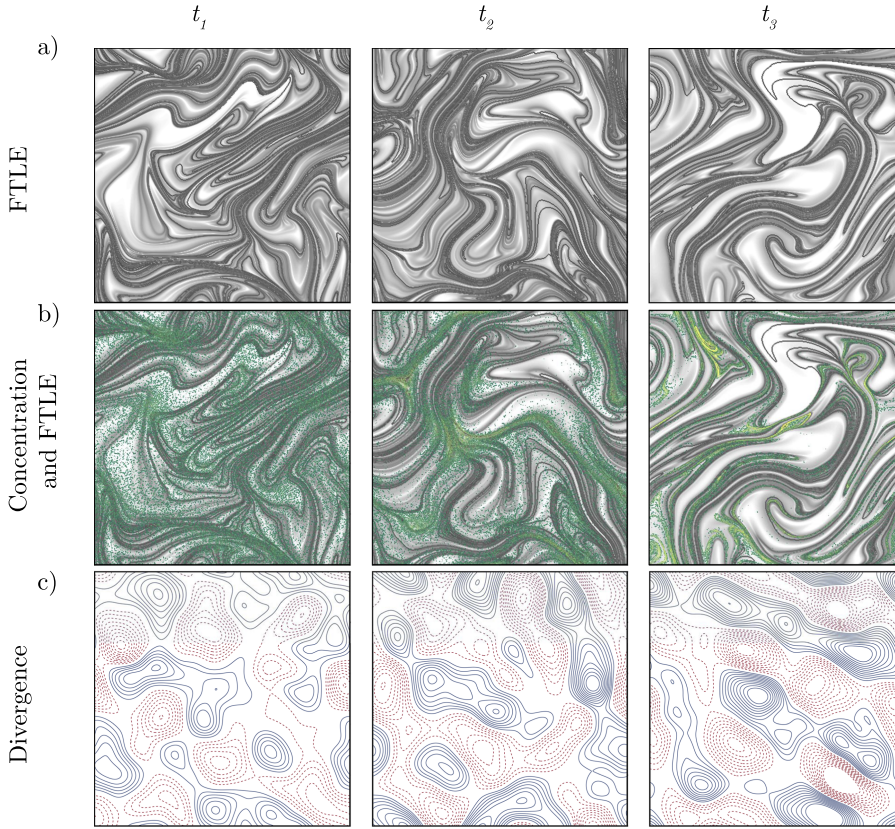


FIG. 11. Clustering and FTLE results for the numerical Taylor vortex flow. (a) FTLE field at times  $t = 0.5$ ,  $t = 2.5$ , and  $t = 15$  (from left to right). (b) Concentration contours from the non-divergence-free Taylor vortex model with concentrations ranging from  $C/C_0 = 0.5$  (green) to  $C/C_0 = 6$  (yellow) overlaid on the FTLE field from (a). (c) Divergence field corresponding to times shown in (a) and (b). Red (dashed) contours indicate regions of divergence and blue (solid) contours indicate regions of convergence.

mental data (Sec. III B). Figure 11(c) shows the divergence at times corresponding to times shown in Fig. 11(a). At early times, clusters begin forming in convergent regions of the flow (blue/solid lines), with large voids forming in divergent regions (red/dashed lines). As time progresses, clusters become more compact and are stretched by the surrounding flow. Due to the Eulerian nature of the divergence field, it no longer captures the regions where clusters are present as they now have a complex time history of compression and stretching.

As done in the experimental section, Pearson correlation coefficients between particle concentrations and the FTLE, dilatation, and divergence field are computed [Figs. 12(a)–12(c)]. These results are strikingly similar to those shown in the experimental section (Fig. 9). Both the FTLE and dilatation fields show strong correlations that plateau at approximately 0.5 and 0.75, respectively. The divergence field, meanwhile, has an initially strong correlation as clusters begin to form in the convergent regions of the flow, but then quickly decays as the clusters are continually stretched and deformed by the flow.

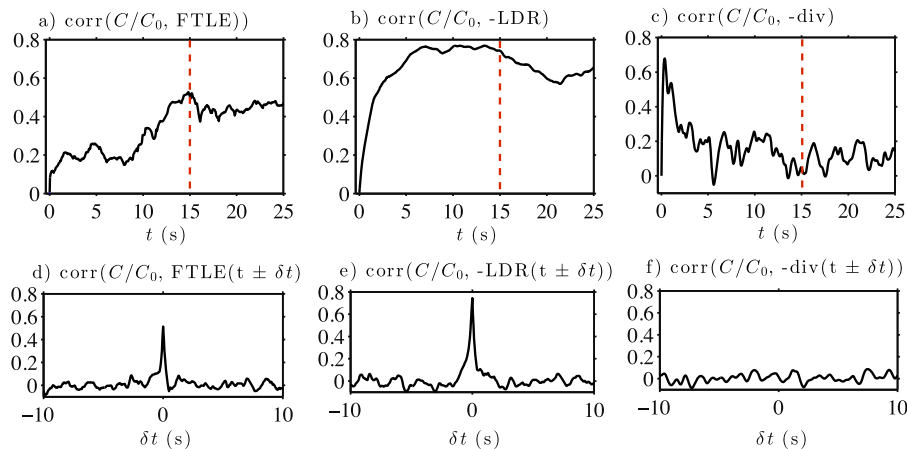


FIG. 12. [(a)–(c)] 2D Pearson correlation coefficients for the numerical Taylor vortex flow between (a) particle concentration ( $C/C_0$ ) and FTLE, (b) particle concentration ( $C/C_0$ ) and Lagrangian dilatation rate (LDR), and (c) particle concentration ( $C/C_0$ ) and divergence field (div) as a function of time. [(d)–(f)] 2D Pearson correlation coefficients between the particle concentration ( $C/C_0$ ) at  $t = 15$  [indicated by the red dashed lines in (a)–(c)] and the (d) FTLE, (e) LDR, and (f) divergence field time shifted by  $\delta t$ . Particles are initially well-mixed at  $t = 0$ . To make all correlations positive, the LDR and divergence field are multiplied by  $-1$ .

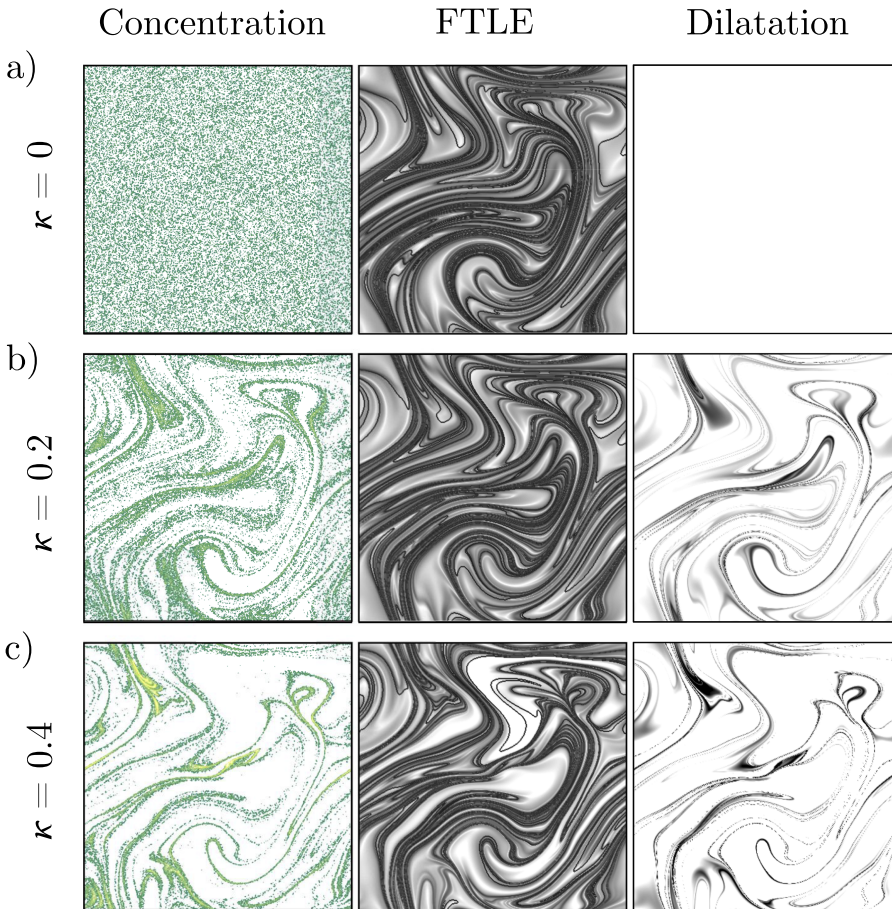


FIG. 13. Concentration (left column), FTLE (middle column), and dilatation (right column) for a single instant of time as a function of increasing compressibility: (a)  $\kappa = 0$ , (b)  $\kappa = 0.2$ , and (c)  $\kappa = 0.4$ .

At these later times, particle concentrations no longer overlap with instantaneous convergent regions of the flow. In addition to these statistics, correlations are computed between the particle concentration at  $t = 15$  and the FTLE, dilatation, and divergence fields time shifted by  $\delta t$  [Figs. 12(d)–12(f)]. A time of  $t = 15$  is chosen as it corresponds with a period of maximum clustering and is shown visually in Fig. 11. The strong spike at  $\delta t = 0$  for both the FTLE and dilatation fields indicates that there is only one unique FTLE/dilatation field that captures particle clustering. Small time shifts between the concentration and FTLE/dilatation field will result in poor overlap. This is not the case with the divergence field, as they are all equally poor.

The FTLE field used as a metric for LCS consists mathematically of the sum of both incompressible straining and compressible dilatation. The incompressible straining component alone is area-preserving and cannot unmix particles to form clusters; dilatation alone initiates the unmixing. Figure 13(a) shows concentration contours (left), the FTLE field (center), and the Lagrangian dilatation rate (right) for an incompressible flow field ( $\kappa = 0$ ). For incompressible, divergence-free flows, clusters do not form and the LCS do not unmix initially well-mixed scalars. The Lagrangian dilatation rate [Eq. (3)] is correspondingly zero throughout the domain, confirming that the flow is area-preserving. When moderate non-divergence-free effects are included [ $\kappa = 0.2$ , Fig. 13(b)], the Lagrangian dilatation rate becomes non-zero and regions of negative dilatation (areas of contraction) coincide with the presence of LCS. Increasing the

compressibility further [ $\kappa = 0.4$ , Fig. 13(c)] leads to larger Lagrangian dilatation rates and increased clustering. In these non-divergence-free cases, the LCS possesses both a dilatation component that results in unmixing and the formation of clusters on the LCS, in addition to a stretching component that subsequently stretches the clusters. Comparing the structure of the LCS in both incompressible and compressible cases, however, there is a dramatic similarity between the two. As compressibility is introduced, the dilatation component of the LCS is strengthened while the structure remains largely unchanged. Without this dilatation component, the LCS cannot create clusters, and scalars remain well-mixed.

#### IV. CONCLUSIONS

Using both an experimental and numerical approach, we have demonstrated that LCS capture the dynamics of clustering in non-divergence-free flows due to the Lagrangian nature of their computation. Conversely, the divergence field is an inferior predictor for the development of voids and clusters due to the fact that it is an Eulerian computation. It should be noted, however, that a non-zero divergence field is required in order for unmixing to occur, even though it may be an inferior metric of predicting where clusters will form as Eulerian metrics do not capture the complex time history of scalar transport. LCS are shown to possess both stretching and dilatation components in non-divergence-free flows that impact scalar clustering. The dilatation component initiates the unmixing

process while the stretching component subsequently deforms the clusters through area-preserving stretching. Therefore, in non-divergence-free flows, the LCS is responsible for both mixing and unmixing of scalars. In scenarios where particles do not begin well-mixed, both of these processes are essential in describing particle transport. This allows LCS, together with the dilatation field, to be used as a template to predict where clusters and corresponding areas of enhanced concentration will form in flows with non-divergence-free behavior. While this research was conducted in a free-surface context where compressibility was the result of particle buoyancy, it should also be applicable to three-dimensional compressible turbulent flows.

## ACKNOWLEDGMENTS

This work was supported by the National Science Foundation (NSF) under Grant No. PHY-1205816 to J.P.C. The authors thank Miguel Calpe for his assistance in coding the jet-firing algorithm and wiring of the jet array used in the turbulence tank.

- <sup>1</sup>J. R. Cressman, J. Davoudi, W. I. Goldburg, and J. Schumacher, "Eulerian and Lagrangian studies in surface flow turbulence," *New J. Phys.* **6**, 53 (2004).
- <sup>2</sup>J. Schumacher and B. Eckhardt, "Clustering dynamics of Lagrangian tracers in free-surface flows," *Phys. Rev. E* **66**, 017303 (2002).
- <sup>3</sup>J. C. Sommerer and E. Ott, "Particles floating on a moving fluid: A dynamically comprehensible physical fractal," *Science* **259**, 335–339 (1993).
- <sup>4</sup>S. Leibovich, "The form and dynamics of Langmuir circulations," *Annu. Rev. Fluid Mech.* **15**, 391–427 (1983).
- <sup>5</sup>J. M. Ottino, "Mixing, chaotic advection, and turbulence," *Annu. Rev. Fluid Mech.* **22**, 207–253 (1990).
- <sup>6</sup>H. Aref, "Stirring by chaotic advection," *J. Fluid Mech.* **143**, 1–21 (1984).
- <sup>7</sup>P. A. Davidson, *Turbulence: An Introduction for Scientists and Engineers* (Oxford University Press, 1999).
- <sup>8</sup>G. Boffetta, J. Davoudi, B. Eckhardt, and J. Schumacher, "Lagrangian tracers on a surface flow: The role of time correlations," *Phys. Rev. Lett.* **93**, 134501 (2004).
- <sup>9</sup>J. K. Eaton and J. R. Fessler, "Preferential concentration of particles by turbulence," *Int. J. Multiphase Flow* **20**, 169–209 (1994).
- <sup>10</sup>W. M. Durham, E. Climent, M. Barry, F. De Lillo, G. Boffetta, M. Cencini, and R. Stocker, "Turbulence drives microscale patches of motile phytoplankton," *Nat. Commun.* **4**, 2148 (2013).
- <sup>11</sup>R. Volk, C. Mauger, M. Bourgoïn, C. Cottin-Bizonne, C. Ybert, and F. Raynal, "Chaotic mixing in effective compressible flows," *Phys. Rev. E* **90**, 013027 (2014).
- <sup>12</sup>J. Larkin, W. Goldburg, and M. M. Bandi, "Time evolution of a fractal distribution: Particle concentrations in free-surface turbulence," *Phys. D* **239**, 1264–1268 (2010).
- <sup>13</sup>J. Larkin, M. M. Bandi, A. Pumir, and W. I. Goldburg, "Power-law distributions of particle concentration in free-surface flows," *Phys. Rev. E* **80**, 066301 (2009).
- <sup>14</sup>J. Larkin and W. Goldburg, "Decorrelating a compressible turbulent flow: An experiment," *Phys. Rev. E* **82**, 016301 (2010).
- <sup>15</sup>S. Lovecchio, C. Marchioli, and A. Soldai, "Time persistence of floating-particle clusters in free-surface turbulence," *Phys. Rev. E* **88**, 033003 (2013).
- <sup>16</sup>H. S. Huntley, B. L. Lipphardt, Jr., G. Jacobs, and A. D. Kirwan, Jr., "Clusters, deformation, and dilation: Diagnostics for material accumulation regions," *J. Geophys. Res.: Oceans* **120**, 6622–6636, doi: 10.1002/2015jc011036 (2015).
- <sup>17</sup>V. Pérez-Muñuzuri, "Mixing and clustering in compressible chaotic stirred flows," *Phys. Rev. E* **89**, 022917 (2014).
- <sup>18</sup>G. Haller, "Lagrangian coherent structures," *Annu. Rev. Fluid Mech.* **47**, 137–162 (2015).
- <sup>19</sup>G. Haller and G. Yuan, "Lagrangian coherent structures and mixing in two-dimensional turbulence," *Phys. D* **147**, 352–370 (2000).
- <sup>20</sup>T. Peacock and J. Dabiri, "Introduction to focus issue: Lagrangian coherent structures," *Chaos* **20**, 017501 (2010).
- <sup>21</sup>W. Tang and C. Luna, "Dependence of advection-diffusion-reaction on flow coherent structures," *Phys. Fluids* **25**, 106602 (2013).
- <sup>22</sup>T. Peacock and G. Haller, "Lagrangian coherent structures: The hidden skeleton of fluid flows," *Phys. Today* **66**(2), 41–46 (2013).
- <sup>23</sup>K. R. Pratt, J. D. Meiss, and J. P. Crimaldi, "Reaction enhancement of initially distant scalars by Lagrangian coherent structures," *Phys. Fluids* **27**, 035106 (2015).
- <sup>24</sup>R. L. Panton, *Incompressible Flow* (John Wiley Sons, Inc., 1996).
- <sup>25</sup>T. Sapsis and G. Haller, "Clustering criterion for inertial particles in two-dimensional time-periodic and three-dimensional steady flows," *Chaos* **20**, 017515 (2010).
- <sup>26</sup>M. Sudharsan, S. L. Brunton, and J. J. Riley, "Lagrangian coherent structures and inertial particle dynamics," *Phys. Rev. E* **93**, 033108 (2016).
- <sup>27</sup>V. Pérez-Muñuzuri, "Clustering of inertial particles in compressible chaotic flows," *Phys. Rev. E* **91**, 052906 (2015).
- <sup>28</sup>E. A. Variano and E. A. Cowen, "A random-jet-stirred turbulence tank," *J. Fluid Mech.* **604**, 1–32 (2008).
- <sup>29</sup>R. Monchaux, M. Bourgoïn, and A. Cartellier, "Preferential concentration of heavy particles: A Voronoï analysis," *Phys. Fluids* **22**, 103304 (2010).
- <sup>30</sup>J. R. Fessler, J. D. Kulick, and J. K. Eaton, "Preferential concentration of heavy particles in a turbulent channel flow," *Phys. Fluids* **6**, 3742 (1994).
- <sup>31</sup>R. Monchaux, M. Bourgoïn, and A. Cartellier, "Analyzing preferential concentration and clustering of inertial particles in turbulence," *Int. J. Multiphase Flow* **40**, 1–18 (2012).
- <sup>32</sup>S. C. Shadden, F. Lekien, and J. E. Marsden, "Definition and properties of Lagrangian coherent structures from finite-time Lyapunov exponents in two-dimensional aperiodic flows," *Phys. D* **212**(3-4), 271–304 (2005).